Quantitative Modeling and Optimization of Magnetic Tweezers

Jan Lipfert, Xiaomin Hao, and Nynke H. Dekker*
Kavli Institute of Nanoscience, Delft University of Technology, Delft, The Netherlands

ABSTRACT Magnetic tweezers are a powerful tool to manipulate single DNA or RNA molecules and to study nucleic acid-protein interactions in real time. Here, we have modeled the magnetic fields of permanent magnets in magnetic tweezers and computed the forces exerted on superparamagnetic beads from first principles. For simple, symmetric geometries the magnetic fields can be calculated semianalytically using the Biot-Savart law. For complicated geometries and in the presence of an iron yoke, we employ a finite-element three-dimensional PDE solver to numerically solve the magnetostatic problem. The theoretical predictions are in quantitative agreement with direct Hall-probe measurements of the magnetic field and with measurements of the force exerted on DNA-tethered beads. Using these predictive theories, we systematically explore the effects of magnet alignment, magnet spacing, magnet size, and of adding an iron yoke to the magnets on the forces that can be exerted on tethered particles. We find that the optimal configuration for maximal stretching forces is a vertically aligned pair of magnets, with a minimal gap between the magnets and minimal flow cell thickness. Following these principles, we present a configuration that allows one to apply $\geq$40 pN stretching forces on $\approx$1-μm tethered beads.

INTRODUCTION

Magnetic tweezers (MT) are a single molecule-technique that makes it possible to apply both forces and torques to biological macromolecules. In a typical configuration (Fig. 1), a DNA or RNA molecule is attached with one end to the surface of a flow cell and with the other end to a superparamagnetic bead that is manipulated by external magnetic fields (1–4).

MT assays have provided unique insights into the function and dynamics of biological macromolecules. Examples include studies of the properties of bare DNA (1,5,6) and RNA (7) and of enzymes that act on DNA or RNA, such as topoisomerases (8–10), helicases (11), and polymerases (12–14). MT have several advantages compared to other single molecule force manipulation techniques, such as optical tweezers or atomic force microcopy (2–4,15,16): They can apply torques to the tethered molecule, they can be used to exert and measure very small forces, down to $\leq$10 fN, and they naturally operate in a constant force mode, without the need for feedback. Additional advantages include the facile extension to parallel measurements of multiple molecules (17), the absence of sample heating and photodamage, and the simplicity and robustness of the experimental implementation.

Both permanent magnets and electromagnets can be used for MT and they offer different advantages and disadvantages. When using electromagnets (18–21), the design of coils and pole pieces and the control of magnetizing currents presents an additional complication compared to the use of permanent magnets. At the same time, electromagnets potentially allow one to apply more complex magnetic field patterns, compared to permanent magnets. Electromagnetic tweezers make it possible, in principle, to position and trap magnetic particles in three dimensions; this, however, requires feedback control (20,21).

In general, the field strengths and gradient forces that can be reached with electromagnetic tweezers are somewhat lower than what is achieved with permanent magnets (3,4,18,20,22). If the primary aim is to apply torque and not force, the field strengths required are smaller and electromagnetic tweezers can be very powerful (23,24). However, many applications require application of both stretching forces and torques. Consequently, most MT studies have employed pairs of permanent magnets (Fig. 1) and we will focus on MT using permanent magnets in this study.

The geometry of the permanent magnets in MT has so far been essentially empirically determined, and the resulting forces have been measured experimentally by monitoring the fluctuations of the tethered particles (1,3,4). While this is a valid approach, it would be desirable to quantitatively predict forces on tethered particles: predictive calculations would allow one to optimize the choice of beads, magnets, and magnet geometry for a given application without the need to extensively test materials and geometries experimentally. Examples where optimization is required include applications that require high forces, e.g., to study overstretching transitions in DNA or the rupture of stable intermolecular bonds. A related goal is to minimize the size of beads necessary to apply forces of ~10 pN, as the temporal resolution of current experimental configurations is limited by the viscous drag experienced by the bead (6).

Here we compute the magnetic fields and the forces applied to superparamagnetic beads by permanent magnets. We employ two separate strategies: for simple geometries, the magnetic fields can be calculated semianalytically by

Submitted December 2, 2008, and accepted for publication March 17, 2009.

*Correspondence: n.h.dekker@tudelft.nl

Editor: Laura Finzi.

0006-3495/09/06/5040/10 $2.00

doi: 10.1016/j.bpj.2009.03.055

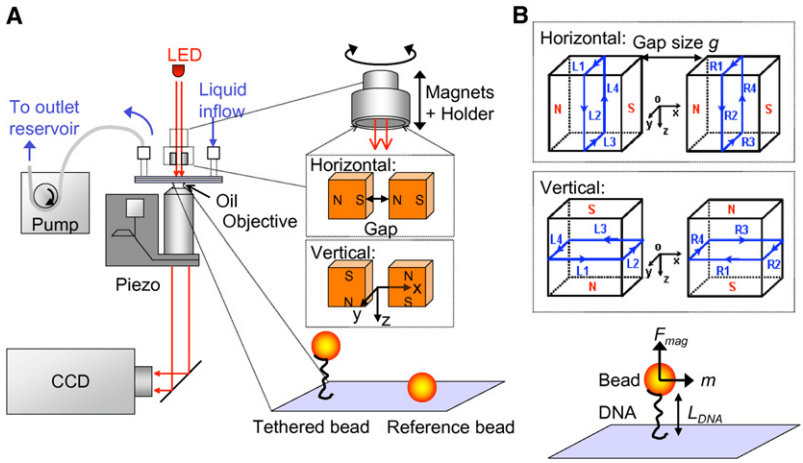

FIGURE 1 Schematic of the magnetic tweezers setup. (*A*) The basic components of the magnetic tweezers setup are shown schematically: the inverted microscope, the CCD camera, the flow cell system with in- and outlet, and the LED illumination. The zoom-ins show the flow cell with a tethered and a reference bead and the magnet pairs in horizontal and vertical geometry. (*B*) The equivalent current loops for the horizontal and vertical magnet geometries that need to be integrated to obtain the total contribution to the magnetic field (see text).

replacing the magnetic dipoles by corresponding current loops and subsequently integrating the contributions to the magnetic field using the Biot-Savart law. Alternatively, we numerically solve the magnetostatic problem in three dimensions using a finite element partial differential equation solver. Numerical solutions can be calculated even for complicated geometries and can take into account material properties, e.g., of magnetically soft iron connecting the magnetic poles, acting as an iron yoke.

We find quantitative agreement between the calculated and simulated magnetic fields and the magnetic fields measured experimentally for different magnet geometries. From the magnetic fields and taking into account the dependence of the beads' magnetization on the external field, we calculate the forces experienced by tethered beads. The predicted forces are in good agreement with the values obtained from measurements on single tethered DNA molecules, after applying a single overall scaling factor to the beads' published magnetization.

Using this ability to quantitatively predict the magnetic forces, we systematically investigate the effects of different magnet geometries and of adding an iron yoke to the magnet configuration. We find that the optimal configuration for maximal stretching forces is a vertically aligned pair of magnets, with one magnetic moment pointing toward the flow cell and one pointing away from it (Fig. 1), with a minimal gap between the magnets and minimal flow cell thickness. For applications that require switching from high to very low forces (<0.1 pN), in contrast, a horizontal magnet configuration with the magnetic moments parallel to the flow cell surface (Fig. 1) and a gap spacing between the magnets of ≈ 1 mm is recommended. For this horizontal configuration the addition of an iron yoke suppressed a region of negative forces, where the bead is pushed away from the magnets, into the flow cell surface. Our results provide general guidelines for the design of MT and we anticipate the theoretical framework presented here to be useful for the systematic optimization of MT for novel applications.

THEORY AND EXPERIMENTAL METHODS

The force experienced by a paramagnetic particle in a magnetic field

The energy of a paramagnetic or superparamagnetic particle in a magnetic field $\vec{B}$ is given by $U = -\frac{1}{2}\vec{m}(\vec{B})\cdot\vec{B}$, where $\vec{m}(\vec{B})$ is the magnetic moment of the particle, which is in turn dependent on the external field. The factor of 1/2 is due to the fact that the magnetic moment is induced by the external field (see (25,26)). The force experienced by the particle is given by the negative gradient of the energy

$$\vec{F} = -\vec{\nabla}U = \frac{1}{2}\vec{\nabla}(\vec{m}(\vec{B})\cdot\vec{B}). \quad (1)$$

For small external fields, the magnetic moment is linear in the external field, $\vec{m} = V_b\chi\vec{B}/\mu_0$, where χ and V_b are the susceptibility and the volume of the bead, respectively. In this case, the force is proportional to the gradient of the square of the magnetic field

$$\vec{F} = \frac{V_b\chi}{2\mu_0}\vec{\nabla}|\vec{B}|^2. \quad (2)$$

For large fields, the magnetic moment of the beads reaches the saturation value $\vec{m}_{sat}$ and the force is proportional to the gradient of the magnetic field

$$\vec{F} = \frac{1}{2}\vec{\nabla}(\vec{m}_{sat}\cdot\vec{B}). \quad (3)$$

To compute the forces experienced by superparamagnetic particles, we therefore need to compute the magnetic field and its gradient, and we require knowledge of the magnetic moment of the beads as a function of the applied field.

Semianalytical calculations of the magnetic fields

The magnetic field from a permanent magnet can be computed using the equivalent source method (27), which relies on approximating the magnet as a distribution of magnetizing currents. In general, a magnetic dipole can be represented by an equivalent current loop, and a permanent magnet can be thought of as consisting of many magnetic dipoles, each represented by its corresponding current loop. For an ideal, homogeneous cubic magnet, the current loops inside the magnet are canceled by adjacent current loops and the magnetization of the magnet is given by a net current along the surfaces of the magnet $\vec{J}_{equi} = \vec{M}\times\hat{n}$, where $\vec{J}_{equi}$ is the equivalent current, $\vec{M}$ is the magnetization of the magnet, and $\hat{n}$ is the surface normal (Fig. 1 *B*). For permanent magnets, the remanent field $\vec{B}_r$ and remanent magnetization $\vec{M}_r$ are related by $\vec{B}_r = \mu_0\vec{M}_r$, and hence the magnitude of the equivalent

current is given by $|\vec{J}_{\text{equi}}| = |\vec{B}_{\text{r}}|/\mu_0$. The contribution of all equivalent currents to the magnetic field at a point in space can be integrated using the Biot-Savart law (26)

$$\vec{B} = \frac{\mu_0}{4\pi}\int J_{\text{equi}}\frac{d\hat{l} \times \hat{r}}{r^2} = \frac{B_{\text{r}}}{4\pi}\int \frac{d\hat{l} \times \hat{r}}{r^2}, \qquad (4)$$

where $\hat{l}$ is a unit vector pointing in the direction of the equivalent current and $\vec{r}$ is the coordinate vector from the element of current to the observation point. The prefactor $B_{\text{r}}/4\pi$ in Eq. 4 depends only on the material properties of the magnet and can be determined experimentally (see below). The integral in Eq. 4 needs to be evaluated over all current loop segments and depends on the magnet geometry. We have numerically evaluated the integral for magnet pairs in different configurations (see Fig. 1 and Results) using MATLAB (The MathWorks, Natick, MA) routines (which are available from the authors on request). Details of the calculations can be found in the Supporting Material.

Numerical three-dimensional simulations of the magnetic fields

The semianalytical approach to computing the magnetic fields outlined in the previous section becomes cumbersome or impossible if more complicated geometries are considered or if material properties like those of an iron yoke have to be included in the calculations. An alternative strategy for computing the magnetic field is to solve the magneto-static problem numerically using finite element methods. In the static case and in the absence of electric fields and external currents, the magneto-static problem for hard ferromagnets (i.e., for magnets with a known, constant magnetization) can be defined as (26)

$$\vec{\nabla} \times (\mu_0^{-1}\vec{B} - \vec{M}) = \vec{\nabla} \times (\mu_0^{-1}(\vec{\nabla} \times \vec{A}) - \mu_0\vec{B}_{\text{r}}) = 0, \qquad (5)$$

where we have introduced the magnetic vector potential $\vec{A}$, which satisfies $\vec{B} = \vec{\nabla} \times \vec{A}$.

We use the AC/DC module of the COMSOL Multiphysics software (COMSOL, Burlington, MA) to solve the partial differential Eq. 5 numerically. Following specification of the model geometry and of the magnetization (or equivalently of the remanent field $\vec{B}_{\text{r}}$), the vector potential $\vec{A}$ is computed numerically for all grid points of the simulation volume (Fig. 2). From solutions of $\vec{A}$, COMSOL computes the magnetic field $\vec{B}$ and its components in a region of interest, which can be exported from the program. All numerical calculations were performed on a dual processor Optiplex 745 workstation (Dell, Round Rock, TX) with 3 GB RAM, with an 80 × 80 × 80 mm outer grid and using the conjugated gradient method. Increasing or decreasing the total simulation volume by 25% did not change the results appreciably. To ensure a sufficient smoothness of the outputted $\vec{B}$ components, we found it necessary to refine the mesh around the region of interest.

Magnetic tweezers experimental configuration

We use a magnetic tweezers setup similar to that developed by Strick et al. (1) (Fig. 1 *A*). Details of our instrument have been described previously (9,28). In brief, a 100× oil immersion objective (N.A. = 1.25) connected to a charge-coupled device (CCD) camera is used to image superparamagnetic beads tethered to the surface of a flow cell. As a tether, we employ a 20.7 kbp DNA construct ligated at the ends to 0.6 kbp DNA PCR fragments that are functionalized with multiple biotin and digoxigenin groups, respectively (28). Flow cells are made from glass microscope coverslips with parafilm spacers and have a total thickness of ≈500 μm. The distance from the inner surface of the bottom slide (where the tethered molecules are attached) to the exterior surface of the top slide (which presents to point of closest approach of the magnets) is ≈400 μm. The bottom surface is coated with polystyrene (1% wt/vol in toluene) and functionalized with anti-digoxigenin (by incubation with 100 μg/mL in phosphate-buffered saline for 24 h at 4°C). Before use, flow cells are incubated for 30 min with bovine serum albumin (10 mg/mL) to passivate the surface. The positions of a DNA-tethered bead and a reference bead attached to the surface are tracked simultaneously at a rate of 120 Hz. From analysis of the CCD images, the bead positions in *x*, *y*, and *z* are determined. After subtraction of the reference bead position to correct for mechanical drift, the tethered bead is tracked with an accuracy of ≈10 nm. From analysis of the bead's fluctuations, the stretching force applied to the tethered bead (the magnetic force pulls the bead away from the surface and toward the magnet pair) can be computed (1,20). Details of the permanent magnets and of the superparamagnetic beads used in our setup are reported in the next sections.

Permanent magnets and magnetic field measurements with a Hall probe

The magnetic fields of different magnet configurations were measured with a KSY 14 Hall probe (Infineon, Munich, Germany) mounted on a manual *x*-*y* translation state. The KSY 14 Hall probe has a thickness of 0.6 mm and was initially calibrated against a model 5080 Gauss meter (Sypris Test & Measurement, Orlando, FL).

We use gold-plated (Ni-Cu-Ni-Au), 5 × 5 × 5 mm neodymium-iron-boron (NdFeB) permanent magnets (W-05-N50-G, Supermagnete, Uster, Switzerland). These magnets have a nominal magnetization of N50, corresponding to a residual magnetic field of B_{r} 1.4–1.46 T (www.supermagnete.de/eng/data_table.php). We find $B_{\text{r}} = 1.24 \pm 0.08$ T from measurements of the surface field with a Hall probe (Fig. S1 in the Supporting Material) and we use this experimentally determined value in the rest of this work. Magnet pairs are mounted in magnet holders custom-made from aluminum or magnetically soft iron. Design drawings of the different magnet holders used in this study are provided in Fig. S2, Fig. S3, and Fig. S4.

Magnetization of MyOne and MagSense beads

As paramagnetic beads, we employ streptavidin-coated Dynal MyOne beads (Invitrogen, Carlsbad, CA) or MagSense beads (MagSense, West Lafayette, IN). MyOne beads have a diameter of 1.05 μm (vendor's specification) and consist of a polystyrene matrix with embedded iron oxide grains (29,30). The nominal diameter of the MagSense beads is 1 μm, but in the microscope image we observe that the MagSense beads appear to be slightly larger than MyOne beads. In addition, MagSense beads exhibit larger size variations from bead to bead.

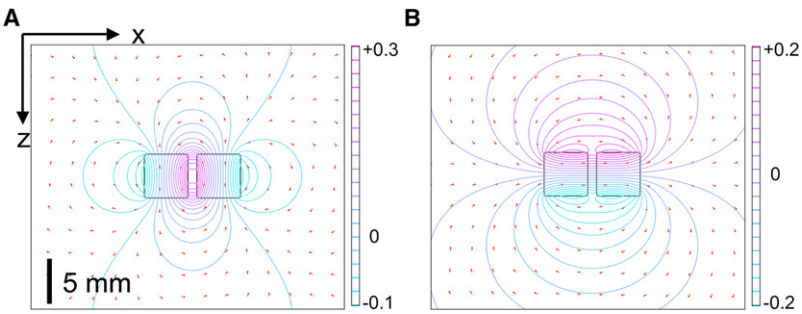

FIGURE 2 Finite element simulations of magnets in the vertical (*A*) and horizontal (*B*) configuration. Numerical three-dimensional calculations were carried out in COMSOL (see Theory and Experimental Methods). For clarity, a two-dimensional cross section of the *x*,*z*-plane through $y = 0$ is shown. The graphs show color-coded iso-contour lines of the *z* component of the magnetic vector potential A_z. The local direction of the magnetic field $\vec{B}$ is indicated by the red arrows.

The magnetic moment of (super)paramagnetic particles as a function of the external field, $\vec{m}(B)$, has a sigmoidal shape and is well described by the Langevin function (3). Magnetization (magnetic moment density) data are supplied by the vendors for both MyOne and MagSense beads (Fig. S5). We fit the vendor-supplied data to a Langevin function

$$M(B) = M_{\text{sat}}\left(\coth(B/B_0) - \frac{1}{B/B_0}\right) \quad (6)$$

with the saturation magnetization M_{sat} and the characteristic field B_0 as fitting parameters and find $M_{\text{sat}} = 43.3$ kA/m (132.4 kA/m) and $B_0 = 12$ mT (31 mT) for MyOne (MagSense) beads (Fig. S5). At low applied fields, the magnetization increases linearly with the external field. However, at fields above ≈ 0.1 T, $\vec{M}(B)$ saturates and approaches M_{sat}.

In this work, we assume that the direction of the magnetic moment is always in the direction of the external field and neglect the small permanent component of the magnetic moment, $\vec{m}_0$, that gives superparamagnetic beads a preferred direction. In certain magnetic tweezers applications this permanent component is crucial, as it allows one to apply torque and to control the beads' rotation (4). However, for beads similar to the ones used in this work, $\vec{m}_0$ has been shown to be much smaller than the induced magnetic moment, $|\vec{m}_0|/|\vec{m}| \leq 0.01$, and hence $\vec{m}_0$ does not significantly contribute to the applied force (31). In addition, we neglect the effect of gravity on the forces acting on the beads (see Supporting Material).

RESULTS AND DISCUSSION

Calculated and simulated magnetic fields are in quantitative agreement with Hall probe measurements

We have computed the magnetic fields from pairs of permanent magnets in two distinct orientations. In the vertical orientation the magnets' moments are antiparallel and point toward and away from the flow cell, respectively (Figs. 1 and 2). In contrast, the horizontal orientation is characterized by aligned magnetic moments, parallel to the surface of the flow cell (Figs. 1 and 2). Both configurations have been successfully used in magnetic tweezers setups. Initially, we will consider cubic magnets of a fixed size, $5 \times 5 \times 5$ mm. In addition to the alignment, an important parameter of the magnet geometry is the gap size g, i.e., the distance between the magnets. The fields are measured and computed along the z axis (Fig. 1), i.e., along the axis of symmetry between the two magnets. The point directly centered between the magnets is taken as the coordinate center; the magnets' surface that limits the closest approach to the flow cell, is, therefore, at a distance of 2.5 mm.

Fig. 3 shows the measured magnetic fields $B_x(z)$ ($B_y \approx B_z \approx 0$) for pairs of magnets in vertical (*brown* and *red symbols*) and horizontal (*light* and *dark blue symbols*) configuration. Fig. 3, *A* and *B*, shows data for $g = 1$ mm and 2 mm, respectively. For $g = 1$ mm, magnet holders made from a nonmagnetic material (aluminum, *data points* in *red* and *light blue*) are additionally compared to data obtained with magnet holders machined from soft iron (*brown* and *dark blue data points*) that effectively act as iron yokes.

The experimental data can be compared to the magnetic fields computed from the semianalytical theory (Fig. 3, *black dashed lines*) and from the corresponding three-dimensional finite element calculations (Fig. 3, *solid lines*, same color code as for the experimental data). For the geometries without iron yokes, semianalytic calculations and the finite element simulations give virtually identical results and are in agreement, within experimental error, with the direct measurements of the magnetic fields. For the geometries with iron yokes, only predictions from numerical calculations were obtained and again show excellent agreement with the experimental measurements (Fig. 3 *A*). The corresponding magnetic field gradients are obtained by finite differencing (Fig. S6). We emphasize that the solid and dashed lines in Fig. 3 are direct theoretical predictions without any free fitting parameters.

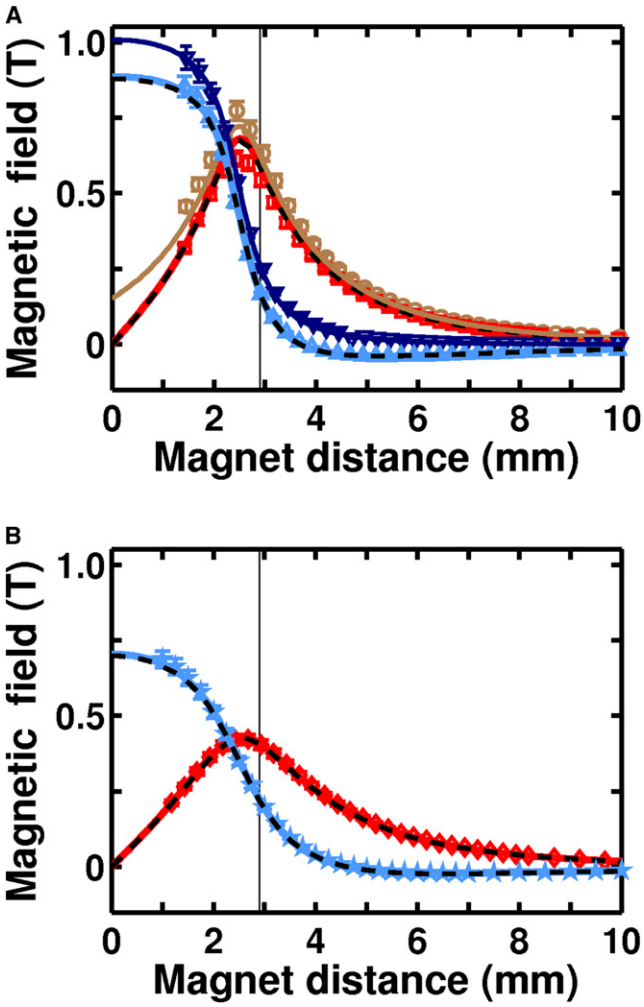

FIGURE 3 Magnetic fields for pairs of permanent magnets. Magnetic fields (in x direction) as a function of distance from the center of magnet pairs (in z direction) in the vertical (*brown* and *red*) and horizontal (*light* and *dark blue*) configuration with a gap size of 1 mm (*A*) and 2 mm (*B*). Data points are from measurements with a Hall probe in the absence (*red* and *light blue*) and presence (*brown* and *dark blue*) of an iron yoke. Solid lines show the results of corresponding calculations using a three-dimensional finite element solver while black dashed lines show the results of semianalytical calculations (see text). The thin vertical lines indicate the position of the flow cell surface in our current setup.

We make several observations: For the vertical magnet configurations and in the absence of an iron yoke, the field is zero in the center between the magnets (as is to be expected from symmetry considerations), maximal at the magnets' surface, and then decays approximately exponentially with increasing distance from the magnets' surface (Fig. 3, *red lines* and *symbols*). In contrast, for the horizontal configuration, the field is maximal at the center between the magnets, exhibits an inflection point at the magnets' surface, and then decreases rapidly with increasing distance (Fig. 3, *blue lines* and *symbols*). For the horizontal configuration without an iron yoke, the field changes sign, i.e., far from the magnet pair it points in the opposite direction as in the gap between the magnets (Fig. 3, *light blue lines* and *symbols*). The addition of an iron yoke suppresses this change in the sign of the field (Fig. 3, *dark blue lines* and *symbols*).

Predictions for the forces on tethered particles

Having obtained quantitative agreement between theoretical calculations and measurements for the magnetic fields, we can compute the force exerted on tethered MyOne superparamagnetic particles using Eq. 1, provided that the dependence of the beads' magnetic moment on the magnetic field is known. The predicted forces can be directly compared to forces measured experimentally from Fourier analysis of the fluctuations of DNA-tethered beads (1,20) (Fig. 1 and Theory and Experimental Methods). Forces were measured experimentally both for $g = 1$ and 2 mm (Fig. 4, *symbols* in panel *A* and *B*, respectively) and in the absence (Fig. 4, *red* and *light blue*) and presence of an iron yoke (Fig. 4, *brown* and *dark blue*). The experimentally accessible range is constrained by the finite thickness of the flow cell ($\approx$400 μm, the excluded region is shown in *gray* in Fig. 4). We find that measurements using different MyOne beads from the same batch give similar results to within 5–10%, similar to the random error from independent repeat measurements of the same bead. The error bars of the forces in Fig. 4 correspond to a relative error of 10% for all data points.

The relative homogeneity of the MyOne beads, both in size and magnetic moment, allows us to treat them as uniform for the purpose of theoretical calculations. Assuming the volume of the beads to be equal to that of a sphere with a diameter equal to 1.05 μm, and using the vendor-supplied volume magnetization as a function of the applied field (fit by a Langevin function, see Theory and Experimental Methods), the predicted forces are systematically too low by ~40%. However, by introducing a single multiplicative scaling parameter, we obtain theoretical predictions from both numerical simulations (Fig. 4, *solid lines*, same color code as above) and semianalytical calculations (Fig. 4, *black dashed lines*) that are in good agreement with the experimentally measured forces over the entire experimental range.

The single scaling parameter was determined to be 1.4 from a global fit to all data points shown in Fig. 4 (fitting

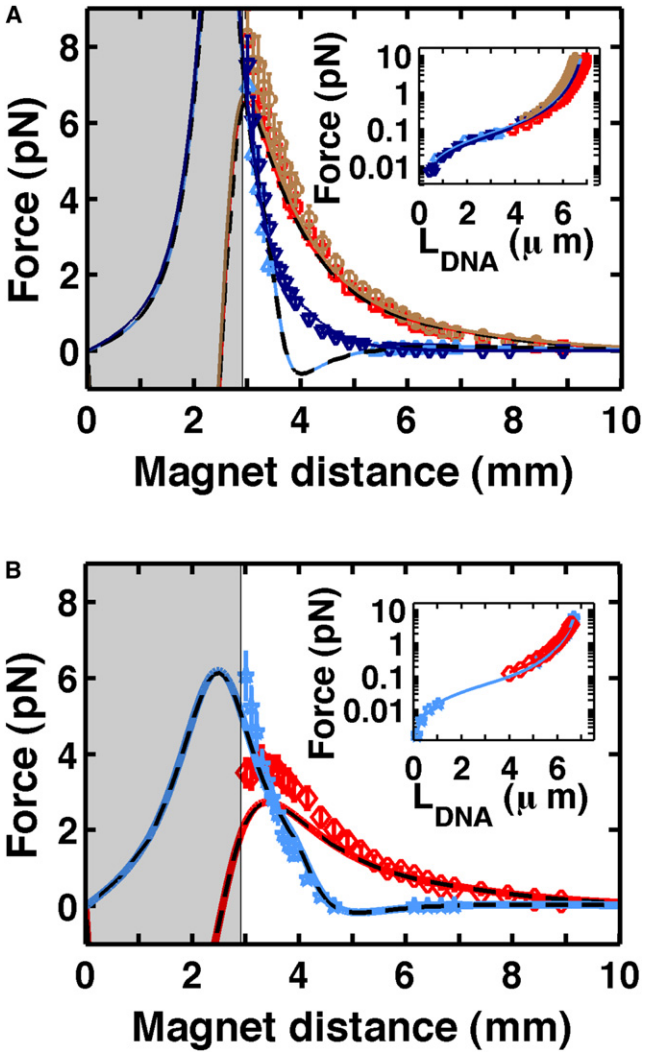

FIGURE 4 Magnetic forces for MyOne beads. The forces are from the analysis of the fluctuations of DNA-tethered beads (*symbols*, same color code as Fig. 3) and theoretical predictions from three-dimensional finite element simulations (*solid lines*, same color code as in Fig. 3) and the semianalytical theory (*black dashed lines*). The main panels shows the forces as a function of magnet position for 1 mm (*A*) and 2 mm (*B*) gap size. Positive values correspond to forces that pull the beads away from the flow cell surface, toward the magnets. The region that is experimentally inaccessible due to the finite thickness of the flow cell is shown as a shaded region in the plot. The insets show the extension of the DNA tethers as a function of force (color code corresponds to the main panels). The solid lines in the inset are fits of the wormlike chain equation using the formula by Bouchiat et al. (35). From the fits, we obtain a contour length of 7.1 $\pm$ 0.2 μm and a persistence length of 47 $\pm$ 4 nm.

to subsets of the data resulted in similar values of the scaling factor, to within $\approx$10%). The need to scale the magnetization might be partially due to the fact that the beads are slightly larger than the vendor-specified value (the fit would be consistent with a diameter of 1.05 μm $\times$ $(1.4)^{1/3}$ $\approx$ 1.17 μm). More likely, however, at least part of the observed discrepancy is due to the fact that the reported measurements of the magnetization as a function of magnetic field (29,30) were obtained from dried bulk samples of the beads. Measurements of

similar beads using micro-machined cantilevers have reported that the magnetization of single beads is systematically higher than the values reported from bulk measurements (32). In the following sections, we consistently use the scaled magnetization for MyOne beads. We note that once this single scaling factor is determined from a measurement, the theory is quantitatively predictive for all other magnet geometries.

The pulling forces that can be applied to MyOne beads using the described magnet configurations and a flow cell with a thickness of 400 μm in either vertical or horizontal geometry are in the range of 10–100 fN to 4–8 pN. Stretching forces of this magnitude are well-suited to the study of DNA phenomena in the entropic stretching regime (33) ($\leq$5–10 pN) where the behavior of DNA is well-described by the wormlike chain model (33–35) (*insets* of Fig. 4, *A* and *B*) and where DNA can be plectonemically supercoiled following the application of torque (33). We observe that the 1-mm gap spacing yields higher forces than the 2-mm spacing, in particular for the vertical magnet geometry (compare Fig. 4, panels *A* and *B*). The effect of g on the achievable forces is discussed in more detail below.

Both the numerical and semianalytical calculations predict a region of negative force for the horizontal magnet configuration in the absence of an iron yoke, i.e., a region where the beads are pushed into the flow cell surface (Fig. 4, *light blue lines* at $\approx$4–5 mm distance). We cannot measure negative or pushing forces experimentally with the current instrument, as the measurement relies on monitoring the fluctuations of a tethered bead. However, we do observe that tethered beads are pushed into the surface in the region that is predicted to yield negative forces, in qualitative agreement with the theoretical predictions.

The effect of an iron yoke on the forces

Interestingly, the finite element simulations predict that the addition of an iron yoke increases the forces only slightly ($<$10%), in good agreement with the experimentally observed forces. The most significant effect of an iron yoke is to suppress the region of negative (or pushing) force in the horizontal configuration. This observation is in line with the finding that the magnetic field in the horizontal magnet configuration does not change sign in the presence of an iron yoke (compare *light* and *dark blue curves* in Fig. 3). Often it is desirable to keep the bead off the surface to avoid unspecific sticking, and under these circumstances the addition of an iron yoke in the horizontal configuration is advantageous. The effect of an iron yoke in the context of varying the gap size is further discussed in the next section.

The effect of the gap size between magnets on forces

Having demonstrated that we can quantitatively predict the forces exerted on magnetic beads for different magnet geometries, we can use this ability to systematically explore a number of magnet designs with a view toward optimizing the magnet geometry for particular applications. First, we study the effect of the gap size g on the forces that can be applied in both the vertical and horizontal magnet geometries.

For the vertical magnet configuration, the force exerted on paramagnetic beads at a given distance increases monotonically with decreasing g (Fig. 5 *A* and its *inset)*. The maximum force that can be applied is attained at a distance $\approx g/2$ from the magnets' surface. For large g, this results in a configuration where the force first increases with increasing sample-magnet distance, then goes through a maximum, and subsequently decreases again (Fig. 4 *B*, *red lines* and *symbols*, and Fig. 5 *A*, *blue lines*). This rollover can be avoided by choosing g small enough so that the region of increasing force with increasing magnet-sample distance is inaccessible ($\leq$1 mm gap for our

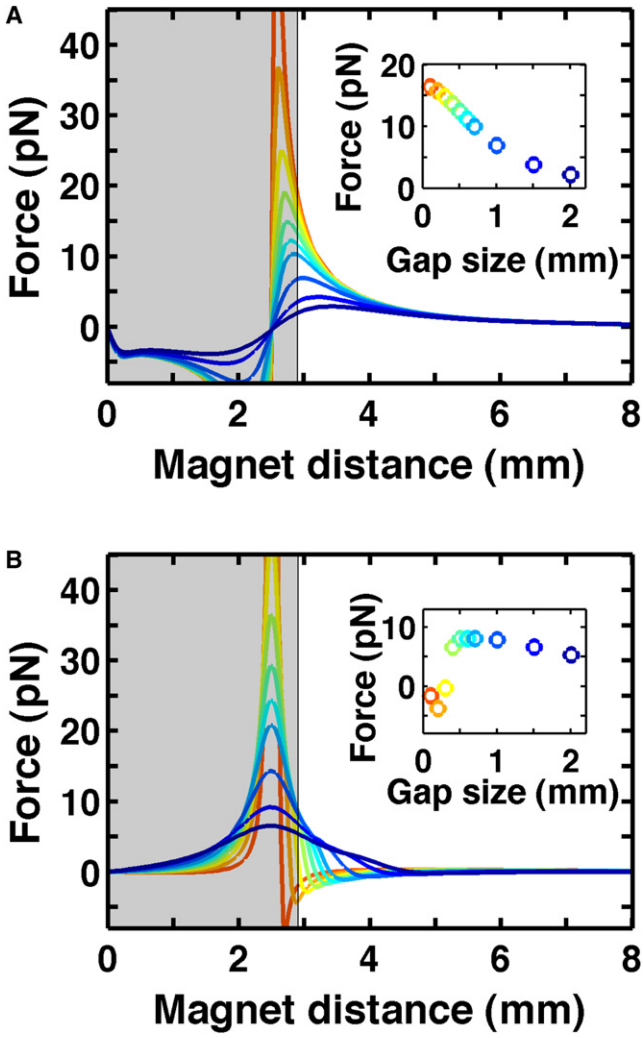

FIGURE 5 Effect of the gap size on force for vertical (*A*) and horizontal (*B*) magnet configurations. Data for magnet configuration in the absence of an iron yoke for gap sizes of 0.1, 0.2, 0.3, 0.4, 0.5, 0.6, 0.7, 1.0, 1.5, and 2.0 mm (color-coded from *red* to *blue*) are computed using the semianalytical model and parameters for MyOne beads. (*Insets*) Force at the point of closest approach for a 400-μm-thick flow cell. The region that is experimentally inaccessible due to the finite thickness of the flow cell is shown as a shaded region in the plots.

400-μm-thick flow cell). For applications that require large stretching forces (or minimal bead sizes for a given stretching force), it is advantageous to use a vertical magnet geometry and to minimize g and flow cell thickness (Fig. 5 *A*). We have followed this strategy and designed a magnet holder with $g = 0.5$ mm. In agreement with the theoretical predictions, we find the maximal force to be increased to $\approx$14 pN for MyOne beads and a 400-μm-thick flow cell (Fig. 7 *A*). From the calculations it is also evident that even modest reductions in the thickness of the flow cell, e.g., by using a thinner spacer between the glass microscope coverslips, can give a substantial increase in the maximum force (see the excluded region due to the finite thickness of the flow cell shown as a *gray region* in Figs. 4 and 5).

For the horizontal magnet configuration, the force shows a more complicated dependence on g (Fig. 5 *B*). The maximum force is attained directly at the magnets' surface, inaccessible due to the finite thickness of the flow cell. In the absence of an iron yoke, there is a region where negative or pushing forces are exerted. The position of the force minimum shifts to smaller distances, closer to the magnets' surface, as g is decreased. At the same time, the absolute value of the negative force increases with decreasing g. For a finite thickness flow cell, the force exerted if the magnets are brought into closest approach to the flow cell's surface shows a nonmonotonic dependence on g (Fig. 5 *B*, *inset*). For the application of maximal force, the optimal g is ~1 mm. A possible advantage of the horizontal configuration is that the magnetic fields and applied forces fall off much more rapidly with increasing distance from the magnets, compared to the vertical configuration. For applications that require us to apply both high and very low forces (<0.1 pN), it can be advantageous to use a horizontal magnet geometry, as it is not always possible to move the magnets far (>10 mm) from the flow cell, due to space or illumination constraints.

We have also examined the effect of gap size g in the presence of an iron yoke (Fig. S7). We find that addition of an iron yoke to the vertical magnet configuration yields only a very modest increase in the force (Fig. S7 *A*). Similarly, the addition of an iron yoke to the horizontal configuration does not tend to increase the maximum force that can be applied significantly. However, it does significantly alter the dependence of the force on the distance from the magnets and completely suppresses the negative force region (Fig. S7 *B*) for all investigated gap sizes. For applications where it is desirable to keep the tethered beads away from the surface to avoid sticking, it is therefore recommended to add an iron yoke to the magnet design. For applications, on the other hand, that benefit from a change in the direction of the force, the horizontal geometry without an iron yoke makes it possible to push beads away from the magnets with forces of up to $\approx$3–4 pN.

We note that for a range of vertical magnet configurations and for horizontal magnet configurations in the presence of an iron yoke, the applied force decreases approximately exponentially with increasing distances from the magnets' surface (Fig. S8). While the exponential dependence is not exact (and clearly inadequate for certain configurations, in particular for the negative force region), it does provide a convenient expression to analyze data in an experimental context and has been used previously (4,36).

The effect of magnet size

We explore how changing the size of the magnets influences the forces on tethered magnetic beads. Fig. 6 shows the forces exerted on MyOne beads by cubic magnets with side lengths from 1 to 20 mm for fixed $g = 1$ mm. Here,

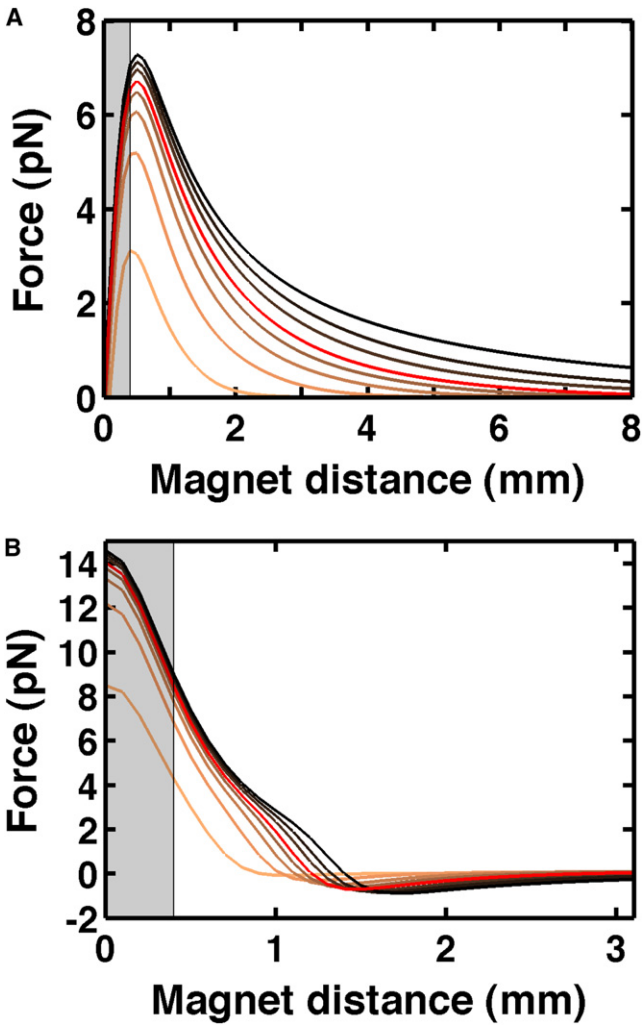

FIGURE 6 Effect of the magnet size on force for vertical (*A*) and horizontal (*B*) magnet configurations (without an iron yoke). Data for cubic magnets of 1, 2, 3, 4, 5, 7, 10, and 20 mm side length (color-coded from *light* to *dark*) was generated using the semianalytical model and parameters for MyOne beads. For ease of comparison, the data for 5-mm side length are shown in red. The distance from the magnets is shown from the magnet surface (and not from the center of the magnets), to aid comparison of differently sized magnets. The region that is experimentally inaccessible due to the finite thickness of the flow cell is shown as a shaded region in the plot.

the distance from the magnets is measured from the magnets' surface (and not from the center of symmetry, in contrast to the previous figures), to aid comparison of the differently sized magnets. The data for the previously considered 5 × 5 × 5 mm magnets are shown in red for ease of comparison (Fig. 6).

For both vertical (Fig. 6 *A*) and horizontal (Fig. 6 *B*) magnet geometries, the forces change appreciably if the magnet size is significantly reduced below 5 mm, e.g., decreasing by more than twofold if the magnet size is reduced to 1 × 1 × 1 mm. In contrast, increasing the magnet size beyond 5-mm side length changes the maximal forces that can be applied comparatively little. For example, increasing the side length to 20 mm yields only <10% higher maximal forces than the 5-mm side length magnets.

While the details of the force dependence on the distance from the magnets (e.g., the decay with increasing distance or the negative force region) depend on the size of the magnets, the maximum applied forces, close to the flow cell surface, do not change appreciably with magnet size, provided that their size is significantly (approximately fourfold) larger than g. The observation that the maximum force does not change appreciably as long as the magnets are significantly larger than the gap size similarly holds for different g and for the case that the magnet dimensions are changed independently (data not shown).

Alternative magnet geometries

We have considered MT geometries using two permanent magnets, in either vertical or horizontal geometry, as these geometries have been utilized in the majority of published MT studies. They provide for robust and straight forward handling of samples and, importantly, permit one to apply torque to the tethered beads. For the magnet configurations considered so far, the force changes appreciably over distances of $\approx$1 mm. Since typical biological applications only involve length changes of ~μm (e.g., a 10 kbp DNA construct has a length of 3.4 μm, when fully extended), measurements are naturally performed in a constant force regime, without the need for electronic feedback.

However, other magnet geometries are certainly possible. For instance, a single permanent magnet (in either vertical or horizontal configuration) is sufficient to apply pulling forces to paramagnetic beads (Fig. S9). In this case, smaller magnets give rise to larger forces close to the magnet's surface, but give a faster fall-off of force with distance from the magnet (Fig. S9). By bringing a sub-mm size magnet very close to the magnetic beads (magnet-sample distances $\leq$50 μm), large forces (~100 pN) can be applied (37). However, bringing the magnet so close to the sample requires an open system, where the magnet is inserted into the experimental buffer. An open system has a number of disadvantages, namely increased mechanical noise, potential evaporation of the buffer, hydrodynamic noise when moving the magnet, and possible chemical reactions at the magnet's surface. In addition, use of a single magnet might require changing the illumination geometry shown in Fig. 1. Finally, we note that the ability to apply torque with a single magnet depends on its orientation: a single magnet in the vertical geometry (Fig. S9) does not permit us to apply torque along the same rotation axis as the other geometries discussed in this work, while a single magnet in the horizontal configuration does.

Another design option for MT is to use shaped pole pieces in combination with permanent magnets. In general, shaped pole pieces can give greater flexibility in the placement of the magnets. A particular example is a MT setup implemented in our laboratory that uses permanent magnets in the horizontal configuration with added pole pieces machined from soft iron. This pole-piece setup has the advantage that one can tilt the magnets and apply stretching forces at varying angles with the flow cell surface (up to $\approx$45°), which can be advantageous as it permits direct imaging of the contour of the stretched DNA (38). With the caveat that we have not explored possible design options for pole pieces exhaustively, so far we did not find an increase of the maximal forces that can be applied through the use of the iron pole pieces, unless they are brought into very close proximity to the beads, which again requires an open system with the disadvantages discussed above.

Optimal choice of beads for magnetic tweezers experiments

The forces that can be applied to tethered beads depend both on the magnet system and the properties of the magnetic beads. We have focused thus far on the magnet geometry, which is justified as the two components can be optimized largely independently. In this section, we briefly discuss aspects that influence the choice of beads. The magnetic moment of the beads entering Eq. 1 is proportional to their volume (Eqs. 2 and 3). For constant volume magnetization, increasing the beads' radius R increases the force very substantially, $\propto R^3$. Applications that require high forces (>50 pN), therefore, typically employ relatively large beads, Dynabeads M-280 (2.8 μm diameter) and M-450 (4.5 μm diameter) being popular choices. However, using large beads has several disadvantages as well. The Brownian forces acting on the beads increase with increasing radius $\propto\sqrt{R}$ and the signal/noise ratio for particle trapping experiments generally decreases (39) as $\propto 1/\sqrt{R}$. In addition, the Stokes friction on moving beads increases linearly with R, posing limits on dynamic measurements. In particular, current measurements of supercoil dynamics are limited by the friction on the tethered bead (rather than by the intrinsic dynamics of DNA supercoils) (6,28).

To increase the forces on a given size bead, a large volume magnetization is desirable, which in turn depends on the magnetic material used and on the fraction of magnetic material in the polymer matrix. MagSense has developed beads

that have a particularly high content of magnetic material, resulting in an approximately threefold larger volume magnetization compared to MyOne beads, as determined from measurements of the dried bulk samples (Theory and Experimental Methods and Fig. S5). We have experimentally measured the forces on MagSense beads with a nominal diameter of 1 μm (Fig. 7 *B*, *symbols*) and find them to be approximately sixfold larger than the forces observed for MyOne beads. The forces predicted for MagSense beads from Eq. 1 using the computed magnetic fields, the vendor-supplied volume magnetization, and assuming a bead diameter of 1.0 μm are too low; however, a reasonable fit is obtained using a single overall scaling factor of ≈ 3.5 (Fig. 7 *B*, *solid line*). The fit is significantly improved if, in addition, the characteristic field B_0 in the expression for the magnetization (Eq. 6) is also allowed to vary (Fig. 7 *B*, *dashed line*). The requirement to scale the computed forces to match the experimentally determined forces is, similar to the case of the MyOne beads, in part likely due to differences in the magnetization of single beads as compared to the dried bulk sample. In addition, we observe MagSense beads to be larger than MyOne beads in the microscope images, and their somewhat larger size likely contributes to the larger experienced forces as well. In short, we find that the use of MagSense beads in combination with vertical magnets with $g = 1$ mm permits measurements with forces in excess of 40 pN using beads only slightly larger than 1-μm diameter.

CONCLUSIONS

We have shown that the forces exerted on tethered superparamagnetic beads by permanent magnets can be calculated from first principles. To obtain quantitative agreement between the predicted forces and experimental measurements from the fluctuations of tethered beads, we found it necessary to introduce a single overall scaling factor. This factor, in part, likely reflects differences between the magnetization of single beads compared to the measurements of dried bulk samples. Chip-based measurements (31,32) of the magnetic properties of single beads have the potential to shed light on these issues in the near future.

We note that once the scaling factor is calibrated experimentally, the theory is quantitative and predictive. We use this ability to predict the forces exerted on superparamagnetic beads to derive a number of recommendations for MT setups. For applications that benefit from large stretching forces, pairs of magnets in the vertical configuration are recommended. For studies that require a rapid decrease of the stretching force with distance from the magnets' surface to permit measurements both at high and very low applied forces, pairs of magnets in the horizontal configuration are optimal. Magnets in the horizontal configuration without an iron yoke make it possible to apply both pulling and pushing forces to superparamagnetic beads. If only pulling forces are desired, it is recommended to add an iron yoke to the horizontal magnet configuration, as it suppressed the change in the sign of the magnetic forces.

This study should serve as a useful guide to experimentalists building new MT setups or seeking to improve an existing MT apparatus. Finally, we hope that these improvements will facilitate new and exciting discoveries regarding the mechanics of nucleic acids and the function and dynamics of protein-nucleic acid interactions.

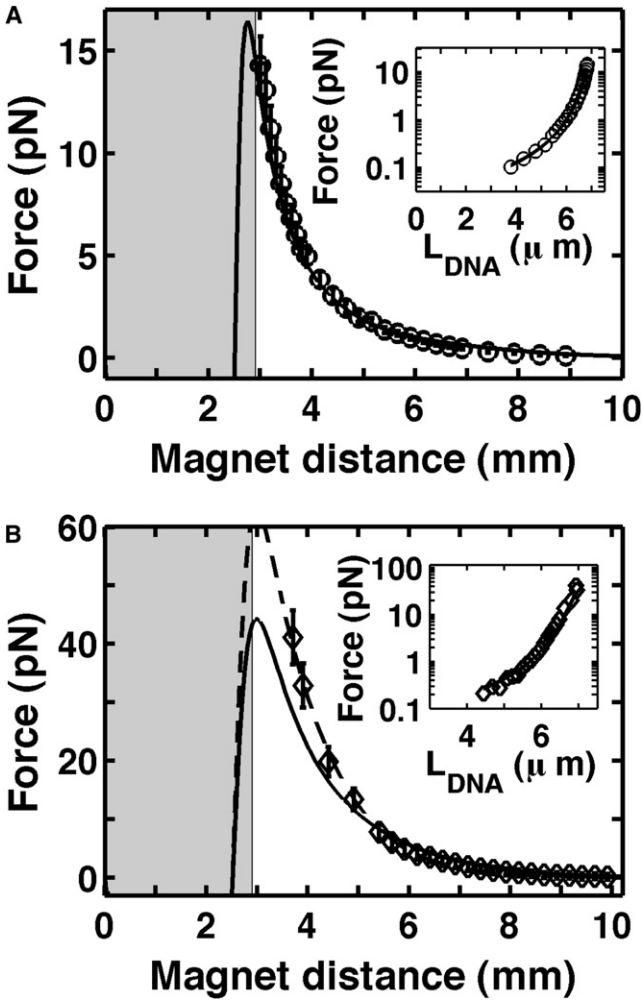

FIGURE 7 Optimized magnet and bead configurations. Forces exerted on MyOne (*A*) and MagSense (*B*) beads by magnets in the vertical configuration with 0.5 mm (*A*) and 1 mm (*B*) gap size. The forces are obtained from analysis of the fluctuations of DNA-tethered beads (*symbols*) and theoretical predictions from the semianalytical theory (*solid line*). For MagSense beads, the fit is improved significantly if the value of B_0 is independently varied (*dashed line* in *B* for $B_0 = 10$ mT); see text. The region that is experimentally inaccessible due to the finite thickness of the flow cell is shown as a shaded region in the plots. We note that for the MagSense bead measurements, we have left out the maximum force region with the magnets close to the flow cell surface, as the large forces experienced there tended to break the attachments of the tether used in our experiments (in particular the anti-dioxigenin-surface bond). (*Inset*) Extension of the DNA tethers as a function of force (for the same data points as in the main panels). The solid lines are fits of the extensible wormlike chain equation using the formula by Bouchiat et al. (35). Using a stretching modulus of 1000 pN for DNA (40), we obtain a contour length of 7.0 μm and a persistence length of 46 nm from the fits.

SUPPORTING MATERIAL

Nine supplementary figures are available at http://www.biophysj.org/biophysj/supplemental/S0006-3495(09)00788-7.

We thank the members of our laboratory, in particular Igor D. Vilfan, Iwijn de Vlaminck, Marijn van Loenhout, Daniel A. Koster, and Aurélien Crut, for stimulating discussions and help with magnetic tweezers measurements, Tom de With for the loan of the Gaussmeter, Pieter Kruit for useful discussions, Jelle van der Does and Jaap Beekman for help with the magnet holders, and Susanne Hage for providing the DNA constructs.

This work was supported by the Nederlandse Organisatie voor Wetenschappelijk Onderzoek (NWO) via its Vidi program and by the European Science Foundation via an EURYI grant.

REFERENCES

1. Strick, T. R., J. F. Allemand, D. Bensimon, A. Bensimon, and V. Croquette. 1996. The elasticity of a single supercoiled DNA molecule. *Science*. 271:1835–1837.
2. Strick, T., J. Allemand, V. Croquette, and D. Bensimon. 2000. Twisting and stretching single DNA molecules. *Prog. Biophys. Mol. Biol.* 74:115–140.
3. Neuman, K. C., T. Lionnet, and J.-F. Allemand. 2007. Single-molecule micromanipulation techniques. *Annu. Rev. Mater. Res.* 37:33–67.
4. Neuman, K. C., and A. Nagy. 2008. Single-molecule force spectroscopy: optical tweezers, magnetic tweezers and atomic force microscopy. *Nat. Methods.* 5:491–505.
5. Strick, T. R., V. Croquette, and D. Bensimon. 1998. Homologous pairing in stretched supercoiled DNA. *Proc. Natl. Acad. Sci. USA.* 95:10579–10583.
6. Crut, A., D. A. Koster, R. Seidel, C. H. Wiggins, and N. H. Dekker. 2007. Fast dynamics of supercoiled DNA revealed by single-molecule experiments. *Proc. Natl. Acad. Sci. USA.* 104:11957–11962.
7. Abels, J. A., F. Moreno-Herrero, T. van der Heijden, C. Dekker, and N. H. Dekker. 2005. Single-molecule measurements of the persistence length of double-stranded DNA. *Biophys. J.* 88:2737–2744.
8. Strick, T., V. Croquette, and D. Bensimon. 2000. Single-molecule analysis of DNA uncoiling by a type II topoisomerase. *Nature*. 404:901–904.
9. Koster, D. A., V. Croquette, C. Dekker, S. Shuman, and N. H. Dekker. 2005. Friction and torque govern the relaxation of DNA supercoils by eukaryotic topoisomerase IB. *Nature.* 434:671–674.
10. Koster, D. A., K. Palle, E. S. Bot, M. A. Bjornsti, and N. H. Dekker. 2007. Antitumor drugs impede DNA uncoiling by topoisomerase I. *Nature*. 448:213–217.
11. Lionnet, T., M. Spiering, S. Benkovic, D. Bensimon, and V. Croquette. 2007. Real-time observation of bacteriophage T4 gp41 helicase reveals an unwinding mechanism. *Proc. Natl. Acad. Sci. USA.* 104:19790–19795.
12. Maier, B., D. Bensimon, and V. Croquette. 2000. Replication by a single DNA polymerase of a stretched single-stranded DNA. *Proc. Natl. Acad. Sci. USA.* 97:12002–12007.
13. Revyakin, A., R. H. Ebright, and T. R. Strick. 2004. Promoter unwinding and promoter clearance by RNA polymerase: detection by single-molecule DNA nanomanipulation. *Proc. Natl. Acad. Sci. USA.* 101:4776–4780.
14. Revyakin, A., C. Liu, R. H. Ebright, and T. R. Strick. 2006. Abortive initiation and productive initiation by RNA polymerase involve DNA scrunching. *Science*. 314:1139–1143.
15. Bustamante, C., Z. Bryant, and S. Smith. 2003. Ten years of tension: single-molecule DNA mechanics. *Nature*. 421:423–427.
16. Bockelmann, U. 2004. Single-molecule manipulation of nucleic acids. *Curr. Opin. Struct. Biol.* 14:368–373.
17. Ribeck, N., and O. A. Saleh. 2008. Multiplexed single-molecule measurements with magnetic tweezers. *Rev. Sci. Instrum.* 79:094301.
18. Haber, C., and D. Wirtz. 2000. Magnetic tweezers for DNA micromanipulation. *Rev. Sci. Instrum.* 71:4561–4570.
19. Bausch, A., F. Ziemann, A. Boulbitch, K. Jacobson, and E. Sackmann. 1998. Local measurements of viscoelastic parameters of adherent cell surfaces by magnetic bead microrheometry. *Biophys. J.* 75:2038–2049.
20. Gosse, C., and V. Croquette. 2002. Magnetic tweezers: micromanipulation and force measurement at the molecular level. *Biophys. J.* 82:3314–3329.
21. Fisher, J. K., J. Cribb, K. V. Desai, L. Vicci, B. Wilde, et al. 2006. Thin-foil magnetic force system for high-numerical-aperture microscopy. *Rev. Sci. Instrum.* 77:023702.
22. Hosu, B. G., K. Jakab, P. Banki, F. I. Toth, and G. Forgacs. 2003. Magnetic tweezers for intracellular applications. *Rev. Sci. Instrum.* 74:4158–4163.
23. Itoh, H., A. Takahashi, K. Adachi, H. Noji, R. Yasuda, et al. 2004. Mechanically driven ATP synthesis by F1-ATPase. *Nature*. 427:465–468.
24. Hirono-Hara, Y., K. Ishizuka, K. Kinosita, M. Yoshida, and H. Noji. 2005. Activation of pausing F1 motor by external force. *Proc. Natl. Acad. Sci. USA.* 102:4288–4293.
25. Lee, H. 2005. Microelectronic/microfluidic hybrid system for the manipulation of biological cells. PhD dissertation, Harvard University, Cambridge, MA.
26. Jackson, J. D. 1999. Classical Electrodynamics, 3rd Ed. John Wiley and Sons, Inc., New York, NY.
27. Bobbio, S., F. Delfino, P. Girdinio, and P. Molfino. 2000. Equivalent sources methods for the numerical evaluation of magnetic force with extension to nonlinear materials. *IEEE T. Mag.* 36:663–666.
28. Crut, A., P. A. Nair, D. A. Koster, S. Shuman, and N. H. Dekker. 2008. Dynamics of phosphodiester synthesis by DNA ligase. *Proc. Natl. Acad. Sci. USA.* 105:6894–6899.
29. Fonnum, G., C. Johansson, A. Molteberg, S. Morup, and E. Aksnes. 2005. Characterization of Dynabeads by magnetization measurements and Mössbauer spectroscopy. *J. Magn. Magn. Mater.* 293:41–47.
30. Derks, R. J. S., A. Dietzel, R. Wimberger-Friedl, and M. W. J. Prins. 2007. Magnetic bead manipulation in a sub-microliter fluid volume applicable to biosensing. *Microfluid Nanofluid.* 3:141–149.
31. Janssen, X. J., A. J. Schellekens, K. van Ommering, L. J. van Ijzendoorn, and M. W. Prins. 2009. Controlled torque on superparamagnetic beads for functional biosensors. *Biosens. Bioelectron.* 24:1937–1941.
32. Koch, S. J., G. E. Thayer, A. D. Corwin, and M. P. de Boer. 2006. Micromachined picoNewton force sensor for biophysics investigations. *Appl. Phys. Lett.* 89:173901.
33. Strick, T. R., M.-N. Dessinges, G. Charvin, N. H. Dekker, J.-F. Allemand, et al. 2003. Stretching of macromolecules and proteins. *Rep. Prog. Phys.* 66:1–45.
34. Marko, J. F., E. D. Siggia, S. Smith, and C. Bustamante. 1994. Entropic elasticity of λ-phage DNA. *Science.* 265:1599–1600.
35. Bouchiat, C., M. D. Wang, J.-F. Allemand, T. Strick, S. M. Block, et al. 1999. Estimating the persistence length of a wormlike chain molecule from force-extension measurements. *Biophys. J.* 76:409–413.
36. Kruithof, M., F. Chien, M. de Jager, and J. van Noort. 2008. Subpico-Newton dynamic force spectroscopy using magnetic tweezers. *Biophys. J.* 94:2343–2348.
37. Yan, J., D. Skoko, and J. F. Marko. 2004. Near-field-magnetic-tweezer manipulation of single DNA molecules. *Phys. Rev. E Stat. Nonlin. Soft Matter Phys.* 70:011905.
38. Deurvorst, Z. 2008. Towards single-molecule measurements of homology search and strand invasion of a RecA-coated ssDNA filament. Master thesis. Delft University of Technology, Delft, The Netherlands.
39. Moffitt, J. R., Y. R. Chemla, S. B. Smith, and C. Bustamante. 2008. Recent advances in optical tweezers. *Annu. Rev. Biochem.* 77:205–228.
40. Smith, S. B., Y. Cui, and C. Bustamante. 1996. Overstretching B-DNA: the elastic response of individual double-stranded and single-stranded DNA molecules. *Science*. 271:795–799.